2001

A Mathematical Model for the Growth of Aluminum Etch Tunnels

Kurt R. Hebert
Iowa State University, krhebert@iastate.edu

A Mathematical Model for the Growth of Aluminum Etch Tunnels

Abstract
A simulation of the growth of pits on aluminum during anodic etching in hot chloride solutions was developed. The simulation is based on equations for mass transport and for the potential-controlled removal of chloride ions from the dissolving surface. The latter process initiates oxide passivation. Etch pits are found to transform into tunnels which at first maintain parallel sidewalls and then begin to taper. The predicted tunnel shapes agree quantitatively with those measured experimentally. Tunnel formation is possible only when the potential at the tunnel entrance during etching is within 20-30 mV of the repassivation potential; as a result, the size of the dissolving surface is nearly constant during pit growth. In the tapered-width regime of tunnel growth, the AlCl3 concentration at the end of the tunnel is near saturation, despite the absence of precipitation from the model equations. The model shows that this condition derives from the low conductivity of the concentrated solution, coupled with the sensitivity of the rate of surface chloride removal to changes in the potential at the dissolving surface.

Keywords
aluminum, etching, anodisation, surface chemistry, reaction kinetics theory, surface topography, electrochemistry, passivation

Disciplines
Chemical Engineering

Comments
This article is from *Journal of the Electrochemical Society* 148 (2001): B236–B242, doi:10.1149/1.1369368. Posted with permission.

Journal of The Electrochemical Society, **148** (6) B236-B242 (2001)
0013-4651/2001/148(6)/B236/7/$7.00 © The Electrochemical Society, Inc.

A Mathematical Model for the Growth of Aluminum Etch Tunnels

Kurt R. Hebert*

Department of Chemical Engineering, Iowa State University, Ames, Iowa 50011, USA

A simulation of the growth of pits on aluminum during anodic etching in hot chloride solutions was developed. The simulation is based on equations for mass transport and for the potential-controlled removal of chloride ions from the dissolving surface. The latter process initiates oxide passivation. Etch pits are found to transform into tunnels which at first maintain parallel sidewalls and then begin to taper. The predicted tunnel shapes agree quantitatively with those measured experimentally. Tunnel formation is possible only when the potential at the tunnel entrance during etching is within 20-30 mV of the repassivation potential; as a result, the size of the dissolving surface is nearly constant during pit growth. In the tapered-width regime of tunnel growth, the $AlCl_3$ concentration at the end of the tunnel is near saturation, despite the absence of precipitation from the model equations. The model shows that this condition derives from the low conductivity of the concentrated solution, coupled with the sensitivity of the rate of surface chloride removal to changes in the potential at the dissolving surface.
 [DOI: 10.1149/1.1369368]

Manuscript submitted December 26, 2000; revised manuscript received February 5, 2001.

Aluminum etch tunnels are corrosion pits formed during anodic etching of the metal in chloride-containing solutions at temperatures above 60°C.[1] Tunnels have square cross sections and widths on the order of 1 μm. They grow by dissolution in the ⟨100⟩ direction, attaining lengths up to 100 μm. The dissolution rate increases with temperature, but remains constant with tunnel length.[2,3] Since the tunnel number density is of order $10^7/cm^2$, tunnel formation is accompanied by a large increase of electrode area. For this reason, the process is used in the manufacture of aluminum electrolytic capacitors. The tunnel tip is a smooth (100) surface, and dissolves at a current density on the order of 10 A/cm^2. On the other hand, there is no detectable change in tunnel width with etching time, indicating that the tunnel walls are effectively passive. The transition between the dissolving tip and passive sidewall surface orientations occurs over a distance smaller than 100 nm. Such an abrupt change of dissolution rate over a small distance can be ascribed to the presence of a protective oxide film on the tunnel walls, but not the tip. As the tunnel grows, the new sidewall surface generated by dissolution is rapidly passivated. Tunnels initiate spontaneously from cubic etch pits, by passivation of the pit sidewalls.

The mechanism of sidewall passivation in tunnels was investigated previously by perturbing the applied etching current with decreasing step and ramp modulations.[4-7] In these experiments, the step or ramp causes the oxide film to cover part of the tunnel tip. In step experiments, passivation occurred in a time of order 1 ms, comparable to the characteristic time of potential decreases accompanying the step, but much smaller than the time for concentration changes to occur.[5,8] Hence, the passivation rate must depend directly on the potential as opposed to factors related to the solution composition.[9] Specifically, the rate of decrease of active area on the tip was shown to be determined by the value of the ''repassivation overpotential,'' η_R. η_R is defined as the difference between the potential which would be measured with a reference electrode at the tip, and the value of the repassivation potential, E_R, corresponding to the composition of the solution adjacent to the tip.[10] E_R is the empirical potential below which pits passivate, and decreases linearly with the logarithm of the chloride concentration.[11]

The rate-controlling step in tip surface passivation was found to be the removal of a surface layer from the tip, which serves to shield the dissolving metal from contact with passivating water molecules.[7] The dependence of E_R on the chloride concentration suggests that the surface layer contains chloride ions, in the form of a monolayer or multilayer film on the dissolving metal. The kinetic expression relating η_R to the rate of removal of the surface layer was identified.[7] The nearly constant tip area during the growth of a tunnel at constant applied current implies that the rate of removal of chloride from this layer is small, so that the number of chloride ions on the tip is not sufficient to cover the new sidewall surface area continuously generated by dissolution. This new surface then rapidly reacts with water to form oxide film.

This passivation model was developed by investigations of tunnels of about 10 μm length, formed in 1 N HCl at 70°C. While these short tunnels have nearly parallel walls, with continued growth their widths would begin to decrease significantly. This tapering becomes more pronounced as the etching temperature is increased. Goad showed that tapered tunnel shapes can be described mathematically by an exponential decay of the tunnel width with length, and that the $AlCl_3$ concentration at the dissolving surfaces of tapering tunnels is close to saturation.[12] From this result, he inferred that a precipitated salt film was present on the dissolving surface, and suggested that the properties of this film controlled the dissolution and passivation phenomena at the tunnel tip. However, for equivalent etching conditions, both the dissolution current density and the (100) etched surface morphology are the same for long tapered tunnels and short ones with parallel walls. Since the dissolving surfaces of the latter tunnels are below saturation, it is not clear how a salt film plays an intrinsic role in tunnel growth. Also, Beck showed that salt film formation on dissolving aluminum does not initiate until the $AlCl_3$ concentration at the surface is 20-40% higher than saturation.[13] On this basis, salt film precipitation might not be expected to occur during tunnel growth.

In the present work, the passivation model of Sinha was incorporated into a mathematical simulation for the shape evolution of etch pits in aluminum, as they evolve into tunnels. Unlike an earlier model of the initial phase of tunnel growth, all phenomena described in the present model are based on independent experimental information, and there are no adjustable parameters.[10] The simulation time was extended so that the lengths of tunnels approached 100 μm, and the predicted width profiles are compared with those measured experimentally by Goad.[12] Since the present model does not incorporate a precipitated salt film on the tunnel tip, this comparison tests whether there might be an alternative explanation for tapered tunnel shapes. It is also relevant to the interpretation of near-saturated solutions in pits, as found in a number of other metal-electrolyte systems.[9,14,15]

Mathematical Model

Model equations.—This section presents the equations of the tunnel simulation. The simulation contains transport equations which predict the concentration and potential distributions in the

* Electrochemical Society Active Member.

cavity, and a kinetic equation which yields the rate of change of dissolving area. The diffusion equation for the $AlCl_3$ binary electrolyte in the tunnel is

$$\frac{\partial C}{\partial t} = D\frac{\partial^2 C}{\partial z^2} - V_d\frac{\partial C}{\partial z} + \frac{\partial \ln a}{\partial z}\left(D\frac{\partial C}{\partial z} - CV_d\right) \quad [1]$$

The terms with V_d, the dissolution velocity, account for the flow of solution into the tunnel to fill the volume vacated by metal dissolution. The last two terms on the right side represent the effect of the variable tunnel cross-sectional area $a(z)$ on the flux. It was shown earlier that the solution in short tunnels can be approximated as a binary electrolyte.[10,16] Also, it was shown recently that despite the very low pH of $AlCl_3$ solutions near saturation, the concentration of hydrogen ion produced by hydrolysis is smaller than 5 mol %, a level which should not introduce significant error into the transport calculations.[17]

Equation 1 does not account for hydrogen gas bubbles inside tunnels, although H_2 gas evolves visibly from the metal surface during etching.[1] Bubbles in tunnels might affect mass transport by inducing flow of the tunnel solution, or obstructing diffusion. However, various authors have provided evidence that diffusion and migration through the unobstructed tunnel are the dominant transport processes. For example, the experimentally supported relationship of the tapered tunnel geometry to a nearly saturated tip solution depends on diffusive mass transport in tunnels.[12,18] The tunnel length dependence of the time constant for the potential decay after current steps is consistent with diffusive transport in the tunnel.[18] Convection and obstruction due to bubbles would be affected significantly by pressure; on the other hand, the tunnel dissolution rate and geometry are independent of pressure over the range 0.3-100 atm.[19] Makino *et al.* used a novel video microscopy technique to observe the interiors of tunnels, and noted that no gas bubbles could be detected during their growth.[3] Finally, Buzza and Alkire studied the growth of corrosion pits in aluminum in alkaline chloride solutions and found that that the dissolution rate is controlled by diffusion, despite visible hydrogen evolution around the pit perimeter.[14] They argued that the Péclet number associated with bubble-induced flow is too small for convection to control the rate of mass transport.

The other model equations govern the current balance, the potential gradient, and the rate of width change. The differential current balance in the tunnel solution is

$$\frac{\partial i_s}{\partial z} + i_s\frac{d \ln a}{dz} = 0 \quad [2]$$

The second term on the left accounts for the effect of the variable cross-sectional area on the solution current density. The potential distribution is written in terms of $\phi(z,t)$, the potential of a Ag/AgCl reference electrode in equilibrium with the local solution, with respect to such an electrode in the bulk solution[20]

$$\frac{\partial \phi}{\partial z} = \frac{i_s}{\kappa} - \frac{4R_gTt_+}{3F}\frac{\partial \ln(Cf_{+-})}{\partial z} \quad [3]$$

The first term on the right side is the contribution of the ohmic potential drop, and the second term is the potential drop due to the concentration gradient. The half-width of the actively dissolving area in the tunnel or pit is denoted by r and its time dependence is governed by the kinetic relationship found by Sinha[7]

$$\frac{dr}{dt} = -k_p \exp\left(-\frac{\alpha F}{RT}\eta_R\right) + \frac{1}{4}k_s r\frac{d\eta_R}{dt} \quad [4]$$

where the kinetic driving force, η_R, is determined by

$$\eta_R = E - \phi|_{z=V_dt} - \left[E_R^b - b\ \log_{10}\frac{C|_{z=V_dt}}{C_b}\right] \quad [5]$$

Table I. Values of model parameters used in simulation.

Bulk $AlCl_3$ concentration	$C_b = 0.333$ M
Cell current density	$i_a = 0.04$ A/cm^2
Temperature	$T = 70$°C
Potential in bulk solution	$E = -0.691$ V
Initial half-width of pit	$r_0 = 0.25$ μm
E_R in bulk solution	$E_R^b = -0.828$ V
Cell ohmic resistance	$R_\Omega = 2.17\ \Omega$ cm^2
Electrolyte diffusivity	$D = 2.1 \times 10^{-5}$ cm^2/s
Aluminum ion transference number	$t_+ = 0.21$
Bulk solution conductivity	$\kappa_b = 0.0186\ (\Omega$ cm$)^{-1}$
Dissolution velocity	$V_d = 1.8$ μm/s
Passivation rate parameters	$k_p = 1.63 \times 10^{-8}$ cm/s $k_s = 7.94$ V^{-1} $\alpha = 4.5$
Péclet number	10^4 Pe = 2.1, 4.0, 7.1 (70, 80, and 90°C)

Here, E is the potential of the aluminum metal *vs.* a Ag/AgCl reference electrode in the bulk solution, b is an empirical constant with the value 0.0337 V,[10] and E_R^b is the repassivation potential at the bulk solution composition C_b. The term in brackets is the value of E_R at the dissolving surface.

The boundary conditions at the tunnel entrance ($z = 0$) are that $C = C_b$ and $\phi = i_aR_\Omega$. At the dissolving surface

$$\left.\frac{\partial C}{\partial z}\right|_{z=V_dt} = \frac{i_d(1 - t_+)}{3FD} \quad [6]$$

It is clear from Eq. 6 that the model does not assume the presence of a salt film on the dissolving surface.

The value of each model parameter was determined from independent experimental data. Electrolyte transport properties (diffusivity, transference number, conductivity) were taken from experimental data for $AlCl_3$ solutions at 70°C.[10,21] D and t_+ were approximated as constants, but the concentration dependence of κ was included explicitly in the model. Two sources for concentration-dependent activity coefficients of $AlCl_3$ were used.[17,22,23] Values of the model parameters are listed in Table I.

Initially, the corroding cavity is depicted as a crystallographic half-cubic etch pit, with depth r_0 and width $2r_0$. These pits are formed within milliseconds after the application of current.[24] The pit bottom is parallel to the outside surface. The electrolyte concentration in the pit is initially C_b, and the entire pit surface is uniformly dissolving. The initial value of r, the half-width of the dissolving surface, is $2r_0$, since it includes the pit sidewalls. At early times, although both the bottom and side faces dissolve, the model geometry is approximated as one-dimensional; *i.e.*, the variables C, i_s, and E depend only on z and t. To account for sidewall dissolution, i_d in Eq. 6 is multiplied by the ratio of the true dissolving area to the pit bottom area: $i_d = i_{d0}A(\text{active})/A(\text{bottom face})$, where i_{d0} is the true (constant) dissolution current density.

The pit-tunnel transition occurs at the point when the pit depth, $r_0 + V_dt$, first exceeds r. The pit or tunnel shape is computed from the time histories of the depth at the passive/active boundary, and of the pit half-width at that point. Prior to the transition, this depth and half-width are $2(r_0 + V_dt) - r(t)$, and $r_0 + V_dt$, respectively. During tunnel growth, the depth at the passive active boundary is $r_0 + V_dt$, and the width is r. At all times, the dissolving surface is assumed to be a flat crystallographic plane.

Dimensionless equations.—The domain of the above model equations changes with time as the tip surface recedes by dissolution. To remove this moving boundary, the equations were rewritten in terms of a dimensionless position coordinate scaled to the pit

depth or tunnel length at a particular time: $x = z/(r_0 + V_d t)$. The other variables were also nondimensionalized. The resulting diffusion equation is

$$(1+\tau)^2 \frac{\partial\theta}{\partial\tau} + (1+\tau)(1-x)\frac{\partial\theta}{\partial x} = \mathrm{Pe}^{-1}\frac{\partial^2\theta}{\partial x^2} + (1+\tau)\frac{\partial \ln A}{\partial\zeta}\left[\mathrm{Pe}^{-1}\frac{\partial\theta}{\partial x} - (1+\tau)\theta\right] \quad [7]$$

where θ is C/C_b, τ is $V_d t/r_0$, ζ is z/r_0, A is a/r_0^2, and the Péclet number Pe is $V_d r_0/D$. The dimensionless versions of Eq. 2-4 are

$$\frac{\partial I}{\partial x} + I(1+\tau)\frac{d \ln A}{d\zeta} = 0 \quad [8]$$

$$\frac{\partial\Phi}{\partial x} = P(1+\tau)\frac{I}{K} - B\left(1 + \frac{d \ln f_{+-}}{d \ln C}\right)\frac{\partial \ln \theta}{\partial x} \quad [9]$$

$$\frac{dR}{d\tau} = -\Psi(\theta|_{x=1})^{-\gamma}\exp(-\sigma\Phi|_{x=1}) - \frac{1}{4}R\left(\frac{\partial\Phi}{\partial\tau}\bigg|_{x=1} - \frac{\gamma}{\sigma}\frac{\partial \ln\theta}{\partial\tau}\bigg|_{x=1}\right) \quad [10]$$

where I is i_s/i_{d0}, Φ is $k_s\phi$, K is κ/κ_∞, and R is r/r_0. The dimensionless groups in Eq. 8-10 are $P = i_{d0}r_0k_s/\kappa_\infty$, $B = 4RTt_+k_s/3F$, $\gamma = b\alpha F/2.303RT$, $\sigma = \alpha F/RTk_s$, and $\Psi = k_p/V_d \exp[-\alpha F/R_gT(E - E_R^b)]$. In the exponential term of Eq. 10, Ψ represents the influence of the bulk potential on the decrease of dissolving area, while $(\theta|_{x=1})^{-\gamma}$ and $\exp(-\sigma\Phi|_{x=1})$ denote the effects of the chloride concentration and potential gradients in the pit, respectively.

The dimensionless boundary conditions at the tunnel entrance are $\theta = 1$ and $\Phi = k_s i_a R_\Omega$. At the dissolving surface

$$\frac{\partial\theta}{\partial x}\bigg|_{x=1} = N(1+\tau)\mathrm{Pe}\ I_d \quad [11]$$

where $N = \rho_{A1}(1 - t_+)/M_{A1}C_b$ and I_d is i_d/i_{d0}. As Eq. 11 shows, use of the reduced position coordinate x causes the boundary at the dissolving surface to be treated as stationary.

Pseudosteady approximation.—As indicated in Table I, the Péclet number is smaller than 10^{-3}. It is shown in this section that the low value of Pe leads to a pseudosteady diffusion approximation, and to the dependence of the rate of decrease of the actively dissolving area on the electrolyte concentration at the dissolving surface. This relation is important in the interpretation of the model results to be given later. The prediction of the tunnel shape according to the pseudosteady diffusion approximation is described in the Appendix.

Since Pe is a small parameter, the solution to the model equations can be expanded as a perturbation series in terms of Pe.[25] For example, the perturbation series for the dimensionless concentration is

$$\theta(x,\tau) = \theta_0(x,\tau) + \mathrm{Pe}\ \theta_1(x,\tau) + \ldots \quad [12]$$

with further terms in ascending powers of Pe. The differential equations governing the zero-order approximation (the functions θ_0, I_0, Φ_0, and R_0) are found by substituting the respective perturbation series into Eq. 7-10 and neglecting terms multiplied by powers of Pe. In terms of the position coordinate, ζ, the equations of the approximate model are

$$\frac{\partial^2\theta_0}{\partial\zeta^2} + \frac{d \ln A_0}{d\zeta}\frac{\partial\theta_0}{\partial\zeta} = 0 \quad [13]$$

$$\frac{\partial I_0}{\partial\zeta} + \frac{d \ln A_0}{d\zeta} I_0 = 0 \quad [14]$$

$$\frac{\partial\Phi_0}{\partial\zeta} = P\frac{I_0}{K} - B\left(1 + \frac{d \ln f_{+-}}{d \ln C}\right)\frac{\partial \ln\theta_0}{\partial\zeta} \quad [15]$$

$$\frac{dR_0}{d\tau} = -\Psi(\theta_0|_{\zeta=1+\tau})^{-\gamma}\exp(-\sigma\Phi_0|_{\zeta=1+\tau}) - \frac{1}{4}R_0\left(\frac{\partial\Phi_0}{\partial\tau}\bigg|_{\zeta=1+\tau} - \frac{\gamma}{\sigma}\frac{\partial \ln\theta_0}{\partial\tau}\bigg|_{\zeta=1+\tau}\right) \quad [16]$$

and the boundary conditions at the tunnel tip are

$$\frac{\partial\theta_0}{\partial\zeta}\bigg|_{\zeta=1+\tau} = N\ \mathrm{Pe}\ I_d \quad [17]$$

and $I_0 = I_d$. The transformed model is equivalent to a pseudosteady approximation for diffusion, since the transient and convective terms of Eq. 7 have been eliminated. This approximation should be accurate in view of the small value of Pe.

The pseudosteady approximation leads directly to a functional dependence of dr/dt on the electrolyte concentration at the dissolving surface. Integration of Eq. 13 and 14 shows that the solution current density, I_0, is equal to $d\theta_0/d\zeta$ multiplied by an integration constant. This constant is evaluated using Eq. 17, yielding a relationship between the local solution current density and concentration gradient

$$I_0 = \frac{1}{N\ \mathrm{Pe}}\frac{\partial\theta_0}{\partial\zeta} \quad [18]$$

Substitution of this expression into Eq. 15 leads to a differential equation for the potential in terms of the concentration, θ_0

$$\frac{d\Phi_0}{d\theta_0} = \frac{P}{N\ \mathrm{Pe}}\frac{1}{K(\theta_0)} - B\left(1 + \frac{d \ln f_{+-}}{d \ln C}\right)\frac{1}{\theta_0} \quad [19]$$

When this equation is integrated, a relationship is found between the tip potential $\Phi_0|_{\zeta=1+\tau}$ and the tip concentration $\theta_0|_{\zeta=1+\tau}$. The exponential term in Eq. 16 can then be viewed as a function of $\theta_0|_{\zeta=1+\tau}$. In other words, for conditions where Pe based on the dissolution velocity is small, this term depends only on the electrolyte concentration at the corroding surface.

Results and Discussion

Despite the accuracy of the pseudosteady approximation for the conditions of tunnel growth, it was not applied in the calculation of model results. It was considered that the solution of the model equations with transient diffusion terms might reveal phenomena whose characteristic length scales may be significantly larger than r_0. Equations 7-10 were integrated numerically using the subroutine D03PKF in the NAG Fortran library. Simulation results at the temperature of 70°C were obtained using the input parameters listed in Table I. Of all the model parameters, the temperature dependence of the dissolution rate should be most significant in its effect on tunnel shapes. Hence, the growth of tunnels at 80 and 90°C was approximated using the transport, kinetic, and thermodynamic properties at 70°C, but the dissolution rate was adjusted according to its established temperature dependence.[1,2,12] The dissolution velocities at 80 and 90°C are 3.4 and 6.0 μm/s, respectively.

In all simulations, the initial half-cubic etch pits evolved into tunnels. Figure 1, which shows the width profile of a tunnel near its entrance, illustrates the cavity shape during the pit-tunnel transformation. The dashed line represents the shape of the etch pit at the

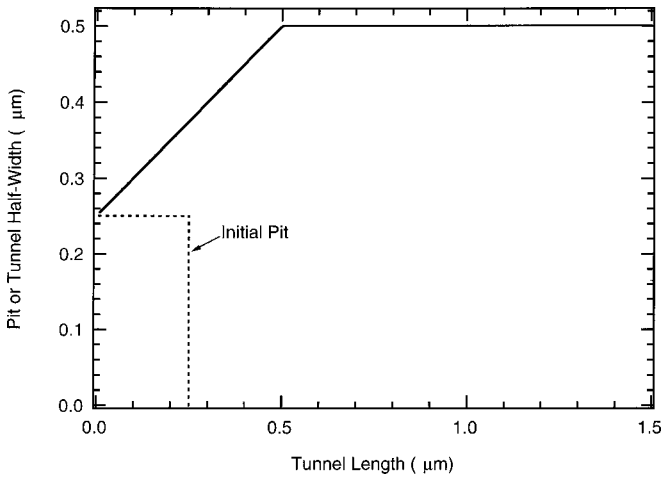

Figure 1. Width profiles of tunnels near their entrances. The solid line represents profiles of tunnels formed at 70, 80, and 90°C. The dashed line is the profile of etch pit at the outset of the simulation.

initiation of the simulation. The same profiles were obtained at the three temperatures of 70, 80, and 90°C. The increasing pit width at depths smaller than 0.5 μm is due to dissolution on the side faces of the tip, which stops at 0.5 μm because at this point the side faces are covered with oxide film. The half-width of the actively dissolving surface is the sum of the pit or tunnel half-width and the length of any actively dissolving surface on the sidewalls. At all times in Fig. 1, the half-width of the actively dissolving surface is the same as that of the initial half-cubic pit, *i.e.*, 0.5 μm. This dimension is constant because η_R is very small, and according to Eq. 4 or 10, the rate of removal of chloride ions from the dissolving surface is negligible. The active-passive boundary moves down the pit sidewall as it expands by dissolution, reaching the bottom face at the time when the half-width of the bottom face is 0.5 μm. The simulation predicts that tunnels will inevitably form from pits, as long as η_R is near zero; this condition is met at potentials near the repassivation potential.

After the tunnels are established, they maintain constant widths for depths of 10-40 μm, and then begin to taper. Figure 2 shows simulated width profiles up to depths of 100 μm, for the three temperatures of 70, 80, and 90°C. It is seen that the depth at which taper commences is about 35 μm at 70°C, but decreases to about 10 μm at 90°C. In the tapering width regime of growth, the width exhibits

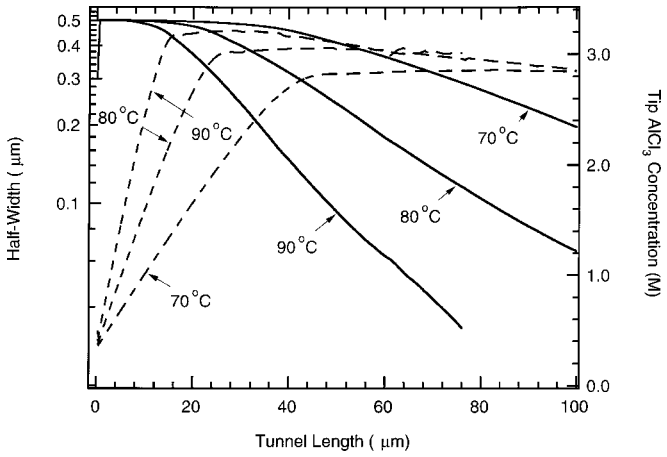

Figure 2. Width profiles of tunnels at 70-90°C (solid lines), along with $AlCl_3$ electrolyte concentration at the dissolving tunnel tip surface (dashed lines).

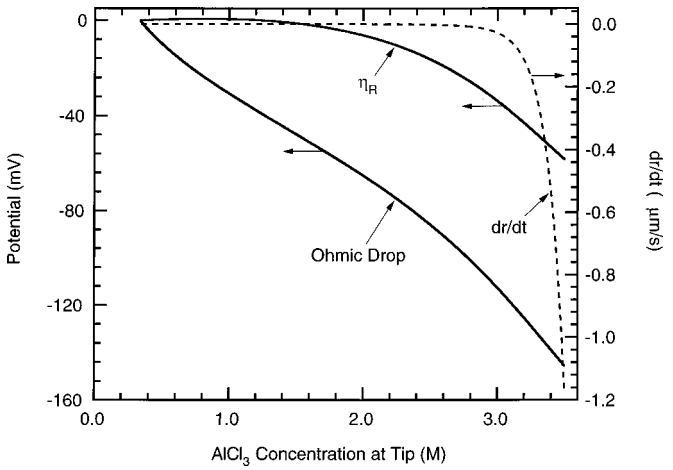

Figure 3. Repassivation overpotential η_R and tunnel ohmic potential drop, plotted as a function of the $AlCl_3$ electrolyte concentration at the dissolving tunnel tip surface (solid lines). Also shown is the rate of decrease of *r*, the half-width of the dissolving surface (dashed line). η_R is found from Eq. 5 and 19, and the ohmic drop is determined by integrating the first term on the right side of Eq. 19. dr/dt is taken from the exponential term in Eq. 4.

an exponential decay with depth. Goad showed that experimentally measured tunnel shapes were also described by exponential decays[12]

$$r(z) = r|_{z=z^*} \exp\left[-\frac{(z - z^*)}{2\lambda}\right] \qquad [20]$$

where z^* is the depth at the initiation of taper and λ is the ''attenuation length,'' and is approximately the same as the tunnel length at the onset of taper. The values of λ from Fig. 2 are 30, 19, and 11 at 70, 80, and 90°C, respectively, compared to the measured values of 36, 22, and 13 μm.[12] Since the measured and predicted attenuation lengths agree within 15%, is clear that the tapering widths predicted by the simulation accurately describe those of actual tunnels.

In addition to the tunnel half-width, Fig. 2 also shows the $AlCl_3$ concentration at the tunnel tip surface as a function of tunnel length. In the constant-width regime of tunnel growth, the tip concentration increases linearly as a function of length, at a rate which increases with temperature. This temperature dependence is expected from the increase of the Al^{+3} ion flux provided by metal dissolution. When the tunnel begins to taper, the tip concentration stops increasing, and remains confined within a narrow range of 2.8-3.2 M. Evidently, while the tunnel grows, its decreasing active area compensates for the increasing length of the diffusion path, resulting in a nearly constant $AlCl_3$ concentration at the tip. In fact, the Appendix shows that an exponential taper is the only shape consistent with both constant current density and constant concentration boundary conditions at the tip. The range of tip concentrations in Fig. 2 agrees closely with 3.1 M, the concentration of a saturated $AlCl_3$ solution.[12,18] Goad noted the connection between tapered tunnels and nearly saturated solutions at the tip, and derived a mathematical expression for λ equivalent to Eq. A-4. While he explained the nearly saturated tip solution by the presence of a precipitated salt film, such a film is not described in the equations of the present model, and so an alternative explanation must be sought.

To interpret the conditions at the dissolving surface which produce taper, the pseudosteady diffusion approximation is considered. Equation 19 was used to calculate the potential at the tunnel tip as a function of the tip electrolyte concentration, and the result was used to determine η_R from Eq. 5. The relation of η_R to tip concentration is independent of the dissolution velocity, so that in the present model it is not affected by temperature. Figure 3 shows that η_R is more positive than −5 mV at concentrations up to about 2 M, but begins to decrease rapidly at higher concentrations. The figure also

shows the tunnel ohmic potential drop, found by integrating the first term on the right of Eq. 19. The downward inflection of η_R above about 2 M parallels that of the ohmic drop, which is caused by the sharp decrease of the conductivity in this range. When the tip concentration is close to saturation (about 3.1 M), the tip potential is 40-50 mV below the repassivation potential, as a result of the low conductivity of concentrated $AlCl_3$ solutions.

The effect of this overpotential on the tunnel shape can be appreciated by examining Eq. 4, which governs the rate of width decay. The exponential and time derivative terms in Eq. 4 were examined separately during the simulations in Fig. 2. It was found that for fully-developed tunnels, the exponential term is at least ten times larger than the time derivative term, and therefore controls the rate of width decrease. This term is plotted in Fig. 3 along with the predicted η_R. Again, this relationship is valid at all etching temperatures. Over a narrow concentration range of 3.0-3.5 M, dr/dt changes dramatically from near zero to about -1.2 μm/s. The latter value would be sufficient to passivate the tunnel completely in a time much smaller than 1 s. As noted above, the same concentration range is present at the tip during the tapering width regime of tunnel growth. When the tip concentration enters this range, the tunnel width begins to decrease, and so the dissolution current decreases. As a result, the tip concentration stops increasing and begins to decrease slightly. From Fig. 3, this causes dr/dt to become smaller, so that the taper rate decreases. Since exponentially tapering tunnels are consistent with a nearly constant tip electrolyte concentration (Eq. A-3), this shape is associated with the ability to vary dr/dt appreciably with small changes of tip concentration.

The presence of a precipitated salt film on the tunnel tip is not necessary to explain the exponential taper and nearly saturated tip solutions of long tunnels. Instead, the simulation indicates that these phenomena are due to the decreasing conductivity at high concentration, coupled with the high sensitivity of dr/dt to changes of the tip electrolyte concentration. The present model for passivation (Eq. 4), which was developed in studies of short tunnels with tips below saturation, additionally predicts the spontaneous transformation of pits to tunnels, and the growth of short tunnels with constant widths. The simulation provides a more complete picture of the tunnel phenomenon compared to models which presuppose a salt film. In addition, Beck showed that $AlCl_3$ concentrations of 120-140% in excess of saturation at a dissolving aluminum surface are required to initiate salt precipitation.[13] On this basis, salt precipitation in tunnels would not be expected, even if the tip concentration is as high as that in Fig. 2.

Two tunnel characteristics which are not manifested in the present results are the approximately 0.1 μm amplitude oscillations of the tunnel width, and the death of long tunnels. The failure to predict wall ripples suggests that they do not result from transient diffusion phenomena coupled to passivation kinetics, as was proposed earlier.[10] It is possible that dr/dt in Eq. 4 is not a smooth function of time as the equation indicates, but is, instead, subject to fluctuations. Such fluctuations could account for sidewall ripples, and also provide a mechanism for tunnel death when the tunnel width has decreased to a value comparable to the characteristic fluctuation size. While fluctuations may formally explain ripples and tunnel death, their physical interpretation is not discussed here.

The effect of electrode potential on tunnel development were explored using the simulation. Figure 4 shows several tunnel profiles at 70°C, for applied potentials ranging from -0.691 to -0.741 V. The cell current density was 40 mA/cm^2 in all cases, resulting in the same cell ohmic drop of 86.8 mV. Hence, the potential variation in the figure produces an equivalent change of the potential at the tunnel entrance. In an actual experiment, changing the applied potential produces different numbers of tunnels, and causes the cell current and ohmic drop to change; the potential at the tunnel entrance cannot be independently adjusted, as is possible in the simulation. Figure 4 indicates that at decreasing potentials, tunnels taper more rapidly; at the three lowest potentials, the tunnel width decreases to zero before it reaches a depth of 100 μm. This behavior is caused by the factor Ψ in Eq. 10, which increases the magnitude of the exponential term contributing to the rate of width decrease as the applied potential is made more negative. It is clear from Fig. 4 that, owing to the strong potential dependence of passivation, long tunnels can be produced at tunnel entrance potentials within about 20-30 mV of E_R. This result is consistent with tunnel entrance potentials derived from measurements, which are found to be very close to E_R and to vary by only about 20 mV during an experiment.[18,25] Since Eq. 4 has not been verified at potentials higher than E_R, this anodic potential range was not investigated with the model.

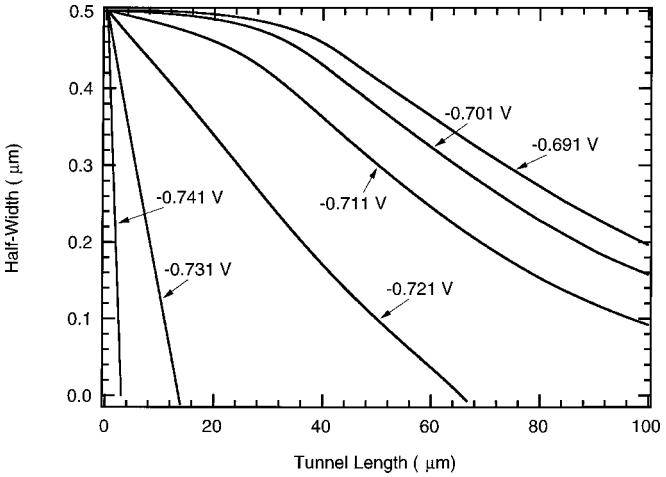

Figure 4. Effect of applied potential (parameter on plot) on tunnel shape profiles at 70°C.

The potential effect in Fig. 4 may be used to interpret tunnel geometries formed by etching in mixed sulfuric-hydrochloric acid baths. The two most evident characteristics of etch morphologies produced in these baths are shorter tunnels compared to HCl baths, and increased surface dissolution around tunnel entrances.[26-28] In fact, sulfuric acid additions are used in industrial etching processes to reduce the maximum tunnel length. The surface dissolution in the mixed baths takes the form of relatively large, irregularly shaped shallow pits. The potential at the entrances of tunnels growing from the surface of such pits would be decreased by an amount equivalent to the pit's ohmic drop. Approximating the pit as a hemisphere, the ohmic drop can be roughly estimated as $3i_{sp}r_{sp}/\kappa$,[4] where i_{sp} and r_{sp} are the surface pit current density and radius. Taking $i_{sp} = 5$ A/cm^2, $r_{sp} = 5$ μm, and $\kappa = 0.5$ $(\Omega$ cm$)^{-1}$,[4] a representative ohmic drop is found to be 15 mV, a value which according to Fig. 4 may significantly reduce the maximum tunnel length. While other effects of sulfuric acid additions on tunnel shape are conceivable, this calculation points out a possible connection between the surface dissolution and short tunnels found after etching in mixed baths.

The dependence of the tunnel shape on the size of the initial cubic pit is depicted in Fig. 5. Results are shown for tunnels at 70°C with initial pit half-widths from 0.15 to 0.5 μm. This range corresponds to the spectrum of pit sizes found in etching experiments at this temperature.[12,24] The tunnel width and tip concentration of short tunnels with parallel walls are not affected significantly by the initial pit size. However, the pit size influences the tapering-width regime of tunnel growth: larger pits are associated with smaller rates of taper (larger λ). The attenuation lengths for the pit depths of 0.15, 0.25, and 0.5 μm are 32, 34, and 36 μm, respectively. The larger λ values are associated with higher tip $AlCl_3$ concentrations in the taper regime (as expected from Eq. A-4 in the Appendix), but the concentration in the constant-width regime is unaffected by r_0. According to Fig. 3, the higher tip concentration is associated with a larger dr/dt for the wide tunnels, but dr/dt as a fraction of the

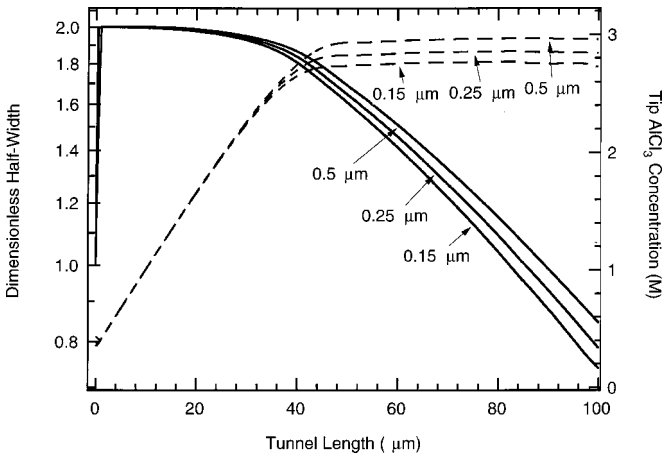

Figure 5. Effect of initial pit depth (or half-width) on tunnel shape profiles at 70°C (solid lines). The dimensionless half-width is normalized using the initial pit depth, r_0. Dashed lines represent the tip electrolyte concentration.

tunnel width is smaller, and thus the value of λ is larger. However, the predicted variability of λ in Fig. 5 is small (±6%), and is not inconsistent with the failure to experimentally observe a dependence of λ on tunnel width for a given set of etching conditions.[12]

The simulation results in Fig. 1-5 were obtained using the empirical activity coefficient correlation due to Meissner.[22] In Fig. 6, the tunnel shape and tip electrolyte concentration at 70°C are compared to those calculated with Pitzer's activity coefficient model.[23] Recently, parameters for the Pitzer model were identified which reproduce experimentally measured activity coefficients of concentrated $AlCl_3$ solutions.[17] Figure 6 shows that the tip concentration and attenuation length in the taper regime are a little larger in the calculations based on the Pitzer model. On the other hand, it is clear that the overall tunnel shape, with its constant width followed by a tapering width, are not affected by the choice of activity coefficient correlation.

Conclusions

A simulation of the growth of pits on aluminum during anodic etching in hot chloride solutions was developed. The simulation is based on mass transport equations, along with an expression for the rate of removal chloride ions from the dissolving surface.[7] Chloride ions are needed to shield the corroding surface from contact with passivating water. Their removal rate is a function of the difference between the potential at the dissolving surface and E_R. Cubic etch pits are found to transform into tunnels because, for the conditions of tunnel growth, the potential is very close to E_R; hence, the rate of removal of chloride ions from the dissolving surface is very small, and the size of the dissolving surface remains constant with time. Predicted tunnel shapes are realistic, in that widths of long tunnels taper exponentially, and those of short tunnels are constant. Tunnel growth is only possible within 20-30 mV of E_R. The exponential taper of long tunnels is due to a nearly constant $AlCl_3$ concentration near saturation at the tip. When the tip solution is nearly saturated, the sharply decreasing conductivity causes the potential at the tip to drop 10-40 mV below E_R, and the passivation rate to become very sensitive to concentration changes. The simulation shows that a nearly saturated solution at the dissolving surface does not necessarily imply the presence of a precipitated salt film which controls dissolution and passivation processes. According to the simulation, the feature of the etching process responsible for the unique tunnel shape is that the potential is within a few millivolts of E_R at all times.

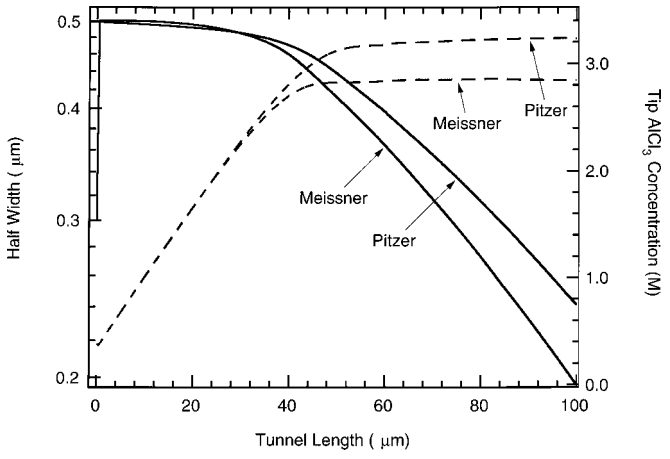

Figure 6. Effect of the activity coefficient correlation used on the tunnel shape profile (solid lines) and dissolving tip surface $AlCl_3$ concentration (dashed lines) at 70°C. The Meissner correlation is from Ref. 21, and the Pitzer correlation is from Ref. 22, with parameters from Ref. 16.

Acknowledgment

The author is grateful for financial support from St. Jude Medical Corp.

Iowa State University assisted in meeting the publication costs of this article.

Appendix

The pseudosteady approximation can be further developed to obtain the tunnel shape profile. Integration of Eq. 13 with the application of the boundary condition at the tunnel tip (Eq. 17) produces the concentration profile $\theta_0(\zeta)$

$$\theta_0(\zeta) = 1 + I_d N \ \mathrm{Pe} \ A_0|_{1+\tau} \int_0^{\zeta} \frac{d\zeta'}{A_0(\zeta')} \qquad [A\text{-}1]$$

As noted earlier, during the initial stage of tunnel growth, η_R is small and so the dissolving area remains constant with time. If A_0 is constant, Eq. A-1 reduces to a linear concentration profile, $\theta_0(\zeta) = 1 + I_d N \mathrm{Pe} \zeta$. In the tapering width regime of tunnel growth, θ is nearly constant at a value near saturation, which is denoted θ*. Setting the left side of Eq. A-1 to the constant θ*, and letting ζ in the upper limit of the integral be $1 + \tau$, yields a relationship between A at $\zeta = 1 + \tau$, and τ (*i.e.*, between the tip area and time). Differentiating that equation with respect to τ produces

$$\frac{d \ \ln \ A|_{1+\tau}}{d\tau} = -\frac{I_d N \ \mathrm{Pe}}{\theta^* - 1} \qquad [A\text{-}2]$$

which upon integration becomes the shape profile of the tapering tunnel

$$A|_{1+\tau} = A^* \ \exp\left[-\frac{I_d N \ \mathrm{Pe}}{\theta^* - 1} \ (\tau - \tau^*)\right] \qquad [A\text{-}3]$$

In dimensional terms, this expression can be written in the form $a = a^* \ \exp[-(z - z^*)/\lambda]$, where the attenuation length is

$$\lambda = \frac{M_{Al} D (C^* - C_b)}{V_d \rho_{Al} (1 - t_+)} \qquad [A\text{-}4]$$

This expression can be compared with the attenuation length (called L) derived by Goad, which was shown to quantitatively describe the tunnel shape.[12] L is the same as Eq. A-4 if the salt film porosity ε in Ref. 12 is set to one.

List of Symbols

A	cross-sectional area of tunnel, dimensionless
a	cross-sectional area of tunnel, cm^2
B	concentration overpotential parameter, dimensionless
b	empirical constant giving dependence of repassivation potential on chloride concentration, 0.0337 V
C	electrolyte concentration, mol/cm^3
C_b	bulk electrolyte concentration, mol/cm^3
D	electrolyte diffusivity, cm^2/s
E	electrode potential of aluminum, V
E_R	repassivation potential, V
E_R^b	repassivation potential at bulk solution composition, V
F	Faraday constant, 96487 C/equiv
f_{+-}	concentration-based electrolyte activity coefficient, dimensionless

I solution current density, dimensionless
I_d model dissolution current density, dimensionless
i_a applied current density, A/cm^2
i_s solution current density, A/cm^2
i_d model dissolution current density, A/cm^2
i_{d0} experimentally measured dissolution current density, A/cm^2
K conductivity, dimensionless
k_p rate parameter for desorption of chloride ions, cm/s
k_s rate parameter for desorption of chloride ions, V^{-1}
M_{Al} atomic mass of aluminum, 27 g/mol
N parameter in boundary condition on dissolving surface, dimensionless
P ohmic resistance parameter, dimensionless
Pe Péclet number, dimensionless
R half-width of actively dissolving surface, dimensionless
R_g gas constant, 8.314 J/(mol K)
R_Ω cell ohmic resistance, Ω cm^2
r half-width of actively dissolving surface, cm
r_0 half-width of initial pit, cm
T absolute temperature (K)
t time, s
t_+ transference number of cation, dimensionless
V_d dissolution velocity, cm/s
x reduced position coordinate, dimensionless
z position coordinate measured from tunnel entrance, cm

Greek

α rate parameter for chloride desorption, dimensionless
Φ potential in solution, dimensionless
ϕ potential in solution, V
γ chloride desorption rate parameter, dimensionless
η_R repassivation overpotential, V
κ conductivity, $(\Omega\ \text{cm})^{-1}$
κ_b bulk solution conductivity, $(\Omega\ \text{cm})^{-1}$
λ attenuation length of tunnel width taper, cm
θ electrolyte concentration, dimensionless
ρ_{Al} density of aluminum, 2.7 g/cm^3
σ chloride desorption rate parameter, dimensionless
τ time, dimensionless
Ψ chloride desorption rate parameter, dimensionless
ζ position coordinate measured from tunnel entrance, dimensionless

References

1. R. S. Alwitt, H. Uchi, T. R. Beck, and R. C. Alkire, *J. Electrochem. Soc.*, **131**, 13 (1984).
2. K. Hebert and R. Alkire, *J. Electrochem. Soc.*, **135**, 2447 (1988).
3. E. Makino, T. Yajima, T. Shibata, M. Ikeda, Y. Tanno, and E. Suganuma, *Mater. Trans., JIM*, **34**, 796 (1993).
4. B. J. Wiersma, Y. Tak, and K. R. Hebert, *J. Electrochem. Soc.*, **138**, 371 (1991).
5. Y. Tak, E. R. Henderson, and K. R. Hebert, *J. Electrochem. Soc.*, **141**, 1446 (1994).
6. Y. Tak and K. R. Hebert, *J. Electrochem. Soc.*, **141**, 1454 (1994).
7. N. Sinha and K. R. Hebert, *J. Electrochem. Soc.*, **147**, 4111 (2000).
8. Y. Tak, Ph.D. Thesis, Iowa State University, Ames, IA (1993).
9. G. S. Frankel, *J. Electrochem. Soc.*, **145**, 2186 (1998).
10. Y. Zhou and K. R. Hebert, *J. Electrochem. Soc.*, **145**, 3100 (1998).
11. J. R. Galvele, in *Passivity of Metals*, R. P. Frankenthal and J. Kruger, Editors, p. 285, The Electrochemical Society, Princeton, NJ (1978).
12. D. Goad, *J. Electrochem. Soc.*, **144**, 1965 (1997).
13. T. R. Beck, *Electrochim. Acta*, **29**, 485 (1984).
14. D. W. Buzza and R. C. Alkire, *J. Electrochem. Soc.*, **142**, 1104 (1995).
15. S. T. Pride, J. R. Scully, and J. L. Hudson, *J. Electrochem. Soc.*, **141**, 3028 (1994).
16. K. R. Hebert, in *Tutorials in Electrochemical Engineering - Mathematical Modeling*, R. F. Savinell, J. M. Fenton, A. West, S. L. Scanlon, and J. Weidner, Editors, PV 99-14, p. 54, The Electrochemical Society Proceedings Series, Pennington, NJ (1999).
17. U. Richter, P. Brand, K. Bohmhammel, and T. Könnecke, *J. Chem. Thermodyn.*, **32**, 145 (2000).
18. K. Hebert and R. Alkire, *J. Electrochem. Soc.*, **135**, 2146 (1988).
19. T. R. Beck, A. J. Babchin, and K. J. McGrath, in *Aluminum Surface Treatment Technology*, R. S. Alwitt and G. E. Thompson, Editors, PV 86-11, p. 334, The Electrochemical Society Proceedings Series, Pennington, NJ (1986).
20. J. Newman, *Electrochemical Systems*, p. 270, Prentice-Hall, Englewood Cliffs, NJ (1991).
21. K. R. Hebert, Ph.D. Thesis, University of Illinois, Urbana, IL (1985).
22. H. P. Meissner, in *Thermodynamics of Aqueous Systems with Industrial Applications*, S. A. Newman, Editor, ACS Symposium Series 133, p. 495, American Chemical Society, Washington, DC (1980).
23. K. S. Pitzer and G. Mayorga, *J. Phys. Chem.*, **77**, 2300 (1973).
24. B. J. Wiersma and K. R. Hebert, *J. Electrochem. Soc.*, **138**, 48 (1991).
25. W. M. Deen, *Analysis of Transport Phenomena*, p. 94, Oxford University Press, New York (1998).
26. J. Scherer, O. M. Magnussen, T. Ebel, and R. J. Behm, *Corros. Sci.*, **41**, 35 (1999).
27. A. Hibino, M. Tamaki, Y. Watanabe, and T. Oki, *Sumitomo Keikinzoku Giho*, **33**, 26 (1992).
28. T. Martin and K. R. Hebert, *J. Electrochem. Soc.*, **148**, B101 (2001).